Available online at www.sciencedirect.com

jmr&t Journal of Materials Research and Technology

journal homepage: www.elsevier.com/locate/jmrt

Original Article

# Photocatalytic high-performance fiber-reinforced cement composites with white Portland cement, titanium dioxide, and surface treated polyethylene fibers

*Hong-Joon Choi* [a,1], *Doo-Yeol Yoo* [a,1], *Gi-Joon Park* [b], *Jung-Jun Park* [b,*]

[a] *Department of Architectural Engineering, Hanyang University, 222 Wangsimni-ro, Seongdong-gu, Seoul, 04763, Republic of Korea*

[b] *Department of Infrastructure Safety Research, Korea Institute of Civil Engineering and Building Technology, 283 Daehwa-dong, Goyangdae-ro, Ilsanseo-gu, Goyang-si, Gyeonggi-do, 10223, Republic of Korea*

ARTICLE INFO

*Article history:*
Received 29 March 2021
Accepted 7 August 2021
Available online 13 August 2021

*Keywords:*
Photocatalyst
High-performance fiber-reinforced cement composites
Titanium dioxide
Nitrogen oxide removal
Polyethylene fiber
Surface treatment

ABSTRACT

In this study, titanium dioxide ($TiO_2$) and polyethylene (PE) fibers were employed to develop photocatalytic high-performance fiber-reinforced cement composites (HPFRCCs). To achieve high $NO_x$ removal capacity, it was necessary to confirm the dispersion of the $TiO_2$ powder. For this purpose, various amounts of viscosity-modifying agent (VMA), ranging from 0% to 1% by weight to cement, were considered along with two types of white Portland cement: Union and Aalborg. Additionally, the PE fiber surface was modified via cold gas plasma and chromic acid treatment to improve the tensile performance of the HPFRCCs. The experimental results indicated that the plastic viscosity of the mortar increases with the addition of VMA. Optimum $NO_x$ removal capacities of 5.72 and 8.10 μmol were respectively achieved for the Aalborg and Union cement types in the mortar at a VMA content of 0.5%. The compressive strength of the tested photocatalytic HPFRCC was approximately 72.7–91.8 MPa. In the case of the hybrid argon (Ar) and oxygen ($O_2$) gases being subjected to plasma treatment, optimum tensile performance—in terms of tensile strength, strain capacity, and *g*-value—was achieved, whereas the samples subjected to chromic acid treatment exhibited poorer tensile performance. Moreover, the single Ar–or $O_2$-gas-based plasma treatment yielded an intermediate tensile performance. The cracking behavior showed trends similar to those of the *g*-value: the hybrid plasma treatment produced the most microcracks because of its high fiber bridging capacity.



* Corresponding author.
E-mail address: jjpark@kict.re.kr (J.-J. Park).
[1] Both authors contributed equally to this work.

https://doi.org/10.1016/j.jmrt.2021.08.027

## 1. Introduction

In addition to global warming, the problem of fine dust is one of the most serious environmental issues focused on by the international community. Although various approaches have been presented to solve these significant issues, it is too early to say whether notable progress has been achieved. An analysis of these issues indicates that the source for most of them is the use of fossil fuels. Burning fossil fuels for energy generation releases several components that cause environmental pollution. In particular, the generation of nitrogen oxides ($NO_x$) is closely related to that of fine dust. $NO_x$ is a generic term used to represent nitrogen monoxide (NO) and nitrogen dioxide ($NO_2$), which react with water vapor present in the atmosphere to form fine dust. In these circumstances, a photocatalyst is considered to be a promising material that can eliminate $NO_x$ under certain conditions. Upon exposure to ultraviolet (UV) light, the photocatalyst material reacts with $NO_x$, which leads to its oxidation and the subsequent production of nitrate ions ($NO_3^-$) as byproducts [1,2]. From the perspective of building materials, architectural engineers have sought to adopt this concept to mitigate $NO_x$ concentration in the atmosphere effectively via the exterior walls of buildings exposed to the atmosphere. Considering the above conditions, many previous studies have adopted titanium dioxide ($TiO_2$) as a photocatalyst. Besides its excellent photocatalytic reactivity, its similar particle size to that of fine aggregates employed in traditional concrete is the most important factor rendering $TiO_2$ powder a suitable construction material [3–5]. An overall conceptual diagram of the photocatalytic reaction occurring through the building walls is presented in Fig. 1.

White Portland cement has been employed in buildings to exploit its advantageous bright color from an aesthetic standpoint. Moreover, this property supports the photocatalytic reaction much more effectively. Rhee et al. [6] reported that ordinary Portland cement exhibits better light absorption capacity than white cement does, leading to the production of fewer electron–hole pairs (EHPs) and achievement of lower $TiO_2$ efficiency. Better $NO_x$ removal performance can be observed in a mixture containing white cement. According to Guo et al. [7], white cement contains less $Fe_2O_3$ than that in ordinary Portland cement. For this reason, concrete with white cement and $TiO_2$ powder exhibits better $NO_x$ removal performance than that of ordinary concrete for the same type and amount of $TiO_2$ powder used.

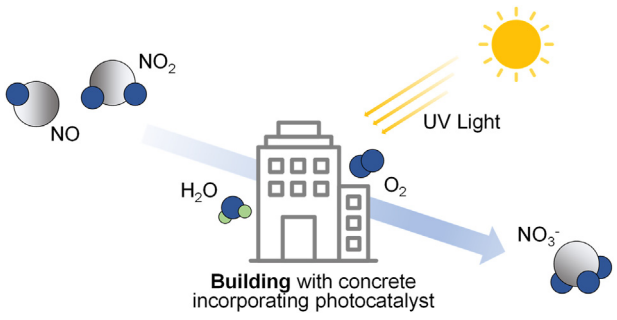


**Fig. 1 – Conceptual description of $NO_x$ removal by $TiO_2$.**

To overcome the limitations of concrete structures (such as curved structures) relying on steel bars [8–10], the use of ultra-high-performance concrete (UHPC) has been proposed. Owing to its high strength and durability, UHPC has also been successfully applied in high-rise buildings and facilities that require a high level of safety [10]. UHPC contains high amounts of steel fibers; under flexural or tensile stress, frictional force is generated between the fiber surface and matrix. Based on these characteristics, steel fibers are used to achieve higher strength and ductility. The steel fibers used most have a positive effect on both the compressive and tensile strengths of UHPC and are excellent substitutes for securing ductility in replacing a portion of the steel rebars. In particular, these materials address the crack and corrosion problems occurring in concrete, which are fatal to steel rebars [11]. Recent studies [12–16] have attempted to increase the friction between the fiber and concrete matrix by means of increasing the surface roughness—e.g., via intentional scratching or coating of the fiber surface. A conventional method is to elicit the chelate effect through an electrolyte solution comprising ethylenediaminetetraacetic acid [16]. Based on the fiber surface modification, superior tensile performance of UHPC can be achieved, such as in terms of tensile strengths of 17.5–20.4 MPa and energy absorption capacities of 106.7–113.0 $kJ/m^3$ [16].

Yoo and Kim [17] reported that the use of polyethylene (PE) fiber as a replacement for a portion of steel fiber is effective for improving the strain capacity and energy absorption capacity of UHPC under tension. Such attempts to modify the fiber surface, particularly by increasing its surface roughness, have also been made for polymeric fibers [18–21]. Some polymeric fibers are further used to improve the hydrophilicity of UHPC. Unlike steel fibers, however, they are hydrophobic and thus develop weak chemical bonds with the surrounding cement matrix. Therefore, if the hydrophilization of polymeric fibers can be addressed, a significant performance improvement can be achieved. Accordingly, from the perspective of high energy absorption capacity, a high-performance fiber-reinforced cement composite (HPFRCC) has been adopted as an eco-friendly exterior building material by incorporating polymeric fibers [22,23].

To date, no study has reported the development of photocatalytic HPFRCCs containing $TiO_2$ powder and surface-treated PE fibers. In this study, rheological analysis was first conducted, and $NO_x$ removal test was performed subsequently. Through these tests, the optimal amount of viscosity-modifying agent (VMA) that improved $NO_x$ removal efficiency was determined. VMA have been commonly used to increase the dispersion of fibers. The fibers evenly distributed over matrix can lead to full saturation of the cracks, improving tensile performance. In addition, it was also considered that the $TiO_2$ powder in the matrix could be distributed uniformly by VMA. Due to the influence of VMA, however, larger and more pores may occur in cement matrix, which can lead to strength reduction of cement composites [24]. In this study, the corresponding property that have been considered weakness in cement research was utilized to $NO_x$ removal. We focused the possibility that the occurrence of pores would increase the probability of $TiO_2$ being exposed to the external conditions, and we observed whether this will lead to

improved $NO_x$ removal capacity according to previous studies [1,5,25,26]. After then, the PE fiber surface was treated using various approaches, such as cold gas plasma and chromic acid treatments, to determine the optimal treatment method in terms of the mechanical properties of an HPFRCC containing photocatalyst $TiO_2$ particles. Finally, the tensile properties of this composite were confirmed via scanning electron microscopy (SEM) image analyses.

## 2. Experimental program

### 2.1. *Material properties and mixture organization*

Two types of white Portland cement were employed: white cement produced by Union Co. and Aalborg Co. (hereafter, the capital letters "U" and "A" indicate the Union white cement and Aalborg white cement, respectively). The physical properties of the two types of white cement and their KS L 5204 standards are listed in Table 1. Although the whiteness index by Hunter was almost the same for both types, the early age (2 days) and 28-day compressive strengths of A were higher than those of U. In addition to cement, silica fume (SF) was also used as a cementitious material. For maintaining a higher denseness and homogeneity, coarse aggregates were not used, while silica flour and sand were adopted as inert filling materials. In addition, NP-600, a highly utilized variant of $TiO_2$ powder, was employed as the photocatalytic material. This material has a particle size similar to that of silica flour and exhibits low reactivity; thus, it can also be used as a filling material [27]. Furthermore, distilled water under a low water-to-binder (W/B) ratio of 0.2 was used. The W/B ratio value indicates the amount of water contained in the superplasticizer (SP). The employed SP was polycarboxylate type, and utilization of this admixture was intended to achieve the self-compacting properties of the mixture. A 19-mm-long PE fiber was mixed with 2% of the total volume of the mixture; the density of the corresponding PE fiber was 0.96 kg/m$^3$. The shape of the fiber is shown in Fig. 2, and its geometrical and physical properties are listed in Table 2.

The variable settings were classified into two categories depending on the test type. The primary objective was to determine the optimal amount of VMA to be mixed into the HPFRCC. Thus, the VMA addition ratio was considered as the primary variable for each test, except for the mechanical experiments. The amounts of VMA incorporated were set to 0.25%, 0.50%, 0.75%, and 1.00% relative to the cement weight, and this material was added to the HPFRCC without replacing other materials [28,29]. Additionally, a plain sample without VMA was prepared as the control sample. Including the control sample, a total of 10 samples were prepared by considering the abovementioned two types of white cement (i.e., U and A). The labeling of the specimens and their mixture details are summarized in Table 3, wherein the percentage of VMA is provided after a hyphen following the cement type. For example, U-0.25% indicates a mortar formed of Union white cement with 0.25% VMA.

**Table 1 – Mechanical properties of several types of white cement and standard for white cement.**

| Mechanical parameter | Unit | KSL5204 Standard | Union | Aalborg |
|---|---|---|---|---|
| Fineness (Blaine) | cm$^2$/g | >3000 | 3400 | 3690 |
| Initial setting time (Vicat) | minutes | >60 | 180 | 148 |
| 2 day strength | MPa | >12.5 | 23.4 | 31.3 |
| 28 day strength | MPa | >42.5 | 46.5 | 64.3 |
| Whiteness (Hunter) | – | >89 | 90.2 | 91.4 |

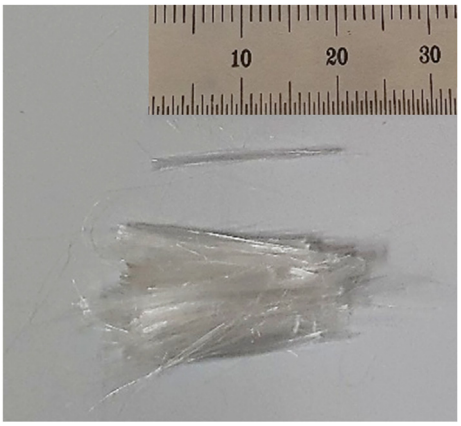


**Fig. 2 – Picture of used PE fiber.**

The secondary objective was to determine the optimal fiber treatment method for the HPFRCCs. The PE fibers were thus incorporated into the mixture, unlike in the previous variable setting, and the optimal amount of VMA was determined by conducting the preceding tests. The amount of fibers mixed in the HPFRCCs was set to a volume fraction of 2%. The other materials used and the mixing ratios were the same as in the previous tests.

The following two types of PE fiber treatment methods were employed: plasma coating and chromic acid oxidation. In the case of the former, all gases and moisture present inside the plasma treatment machine were first removed before the coating process was performed. This is essential for preventing other gases from acting as impurities and for ensuring constant performance of each variable. The treatment was conducted at a low humidity, and argon (Ar) and oxygen ($O_2$) gases were used in the plasma coating. From the standpoint of the type and utilization ratio of the gases, methods involving 100% Ar utilization, 100% $O_2$ utilization, and utilization of a mixture of 50% Ar and 50% $O_2$ were employed. In the case of the latter treatment, the PE fiber reacted with activated chromic acid to regulate the roughness of the fiber surface. The reaction time determines the roughness of the PE fiber, and an optimum reaction time should be set, as the PE fiber burns or is considerably damaged if it reacts excessively. Devaux and Cazé [30] reported that a PE fiber surface can be considerably modified upon its immersion in a chromic acid solution for 10 min. Therefore, in this study, methods for reaction in chromic acid for 5 and 10 min were explored.

**Table 2 – Geometrical and physical properties of PE fiber.**

| Fiber classification | Diameter, $d_f$ [mm] | Length, $l_f$ [mm] | Aspect ratio [$l_f/d_f$] | Density [g/cm$^3$] | Tensile strength [MPa] | Elastic modulus [GPa] |
|---|---|---|---|---|---|---|
| PE fiber | 0.03 | 18 | 600 | 0.97 | 3,000 | 88 |

## 2.2. Experimental methods

### 2.2.1. Rheological test

Several models can be used to measure the fluid viscosity. In this study, the Bingham model was used for this purpose. In this model, the stress applied to a fluid and its moving speed are called shear stress ($\tau$) and shear rate ($\dot{\gamma}$), respectively. Shear rate occurs when the shear stress exceeds a certain value (called yield stress), which indicates that the fluid has started moving. When a fluid is moving, its viscosity affects its movement, and the shear stress and shear rate increase proportionally under ideal circumstances. Plastic viscosity indicates the relation between shear stress and shear rate and can be calculated from the slope of the shear stress–rate ($\tau - \dot{\gamma}$) curve presented in Fig. 3a [19]. A rheometer was used for the viscosity measurement test, as shown in Fig. 3b, and to calculate the shear stress corresponding to the shear rate of each variable. The shear rate was set to increase linearly by means of steadily increasing the rotation speed of the rheometer, and the shear rate was set to range from 15 to 30 $s^{-1}$. In this test, a curing process was not required. After dry and wet mixing for 10 min each, the viscosity was immediately measured by considering the mixture hardening, and the measurement time was set to 5 min. As a result, the shear stress–rate curves for each variable were drawn through the process, and the average slope was calculated using linear regression.

### 2.2.2. Mixing process

Because a larger-capacity mixing process was required compared to those needed in previous tests, mixing was performed using a 20-L-capacity Hobart-type mixer. For a uniform distribution of materials, dry materials, including cement, SF, silica flour, silica sand, and $TiO_2$ powder, were stirred at a low speed for 10 min and then mixed at a high speed for an additional 10 min after addition of water and SP. As the mixing process showed proper flexibility, the PE fiber was inserted, and stirring was performed again at a high speed for 5 min to complete the mixing.

### 2.2.3. Fiber surface treatments

PE fibers exhibit hydrophobic characteristics and thus exhibit poor adhesion to the cement matrix and dispersibility [31]. Thus, for improving its wettability, the fiber surface was modified via cold gas plasma and chromic acid treatments. For the former treatment, two types of inert and reactive gases, Ar and $O_2$, were adopted at a frequency of 40 kHz and power level of 120 W for 2 min. This condition was determined as per the study of Felekoglu et al. [32], who indicated that a 2-min plasma treatment can sufficiently enable the wetting angle to converge to the lower limit at a frequency of 40 kHz and power level of 120 W or higher. The size of the plasma chamber was 500 mm × 500 mm × 500 mm. A vacuum rotary pump with a capacity of 660 LPM was used to facilitate a low-vacuum condition; once the background pressure in the chamber reached $7.0 \times 10^{-2}$ torr, 100 cc of gas was added. Then, the plasma was activated at a working pressure of $2.2–2.5 \times 10^{-1}$ torr.

Devaux and Cazé [30] reported that the PE fiber surface can be modified via immersion in a chromic acid solution for 10 min, whereby the surface roughness is increased from 18.3 to 49.7 nm. Thus, in this study, a chromic acid solution was prepared based on a mixture of potassium dichromate ($K_2Cr_2O_7$), distilled water ($H_2O$), and sulfuric acid ($H_2SO_4$), as follows: $K_2Cr_2O_7$:$H_2O$:$H_2SO_4$ = 4.4:7.1:88.5. After $K_2Cr_2O_7$ and $H_2O$ were mixed together, $H_2SO_4$ was added to the solution and the entire mixture was stirred. The pristine PE fibers were immersed in the chromic acid solution for 5 and 10 min at 20 °C (room temperature). They were then removed from the solution and cleaned using methanol and distilled water for

**Table 3 – Labeling and mixture details of HPFRCGs with various amount of viscosity agent.**

| Specimen | Cement type | Mix proportions [kg/m$^3$] | | | | | | | | W/B[b] |
|---|---|---|---|---|---|---|---|---|---|---|
| | | Cement | Silica fume | Silica sand | Silica flour | $TiO_2$ powder | Viscosity agent | Water | SP[a] | |
| U-Plain | Union | 788.5 | 197.1 | 867.4 | 59.2 | 177.4 | 0 | 160.3 | 52.6 | 0.2 |
| U-0.25% | | | | | | | 1.97 | | | |
| U-0.50% | | | | | | | 3.94 | | | |
| U-0.75% | | | | | | | 5.91 | | | |
| U-1.00% | | | | | | | 7.89 | | | |
| A-Plain | Aalborg | | | | | | 0 | | | |
| A-0.25% | | | | | | | 1.97 | | | |
| A-0.50% | | | | | | | 3.94 | | | |
| A-0.75% | | | | | | | 5.91 | | | |
| A-1.00% | | | | | | | 7.89 | | | |

[a] Superplasticizer includes 30% solid (= 15.8 kg/m$^3$) and 70% water (= 36.8 kg/m$^3$).
[b] W/B is calculated by dividing total water content (160.3 kg/m$^3$ + 36.8 kg/m$^3$) by total amount of binder (788.5 kg/m$^3$ + 197.1 kg/m$^3$).

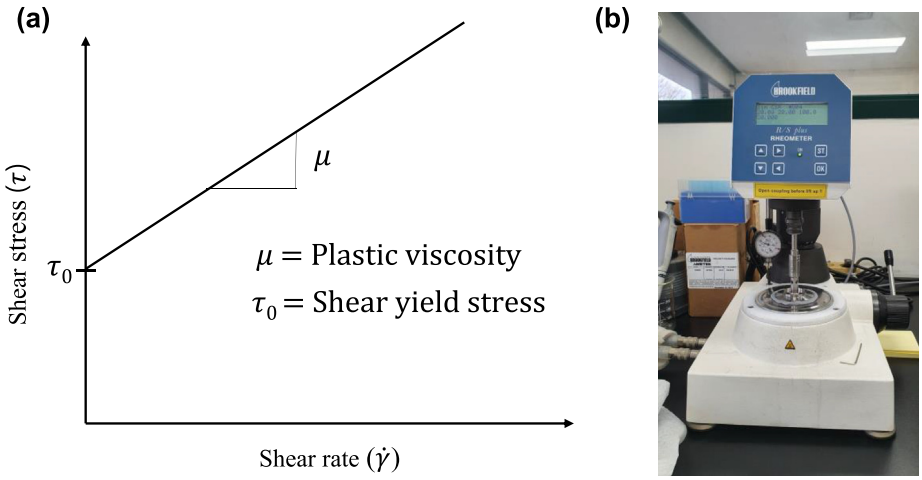


**Fig. 3 – (a) Rheology concept and (b) test setup.**

15 min or more until their original color was restored. Finally, they were dried in air for 24 h before being used for mixing.

The letters "P" and "Cr" denote plasma and chromic acid treatments, respectively. The letters "Ar," "$O_2$," and "Hy" after a hyphen in the case of plasma treatment indicate Ar-, $O_2$-, and hybrid gas-based plasma treatments, respectively. The numbers of 5 and 10 appearing subsequently in the case of chromic acid treatment indicate the treatment time. For example, P-Hy denotes a PE fiber sample having undergone hybrid Ar and $O_2$-based plasma treatment.

### 2.2.4. *NO removal test*

The $NO_x$ removal test was performed in accordance with the ISO 22197-1 standard [33]. For this test, panel specimens were fabricated with dimensions of 50 × 100 × 10 $mm^3$. As mentioned above, the curing procedure involves 48 h of dry curing and 7 days of moisture curing in a water tank at 40 °C. In addition, scratches were intentionally created on the surface of each specimen to achieve better performance. This surface treatment enabled more efficient absorption of $NO_x$ [6,34]. The specimen was exposed to UV radiation within the removal performance evaluation device because the photocatalysts react to reduce NO concentration. The removal performance was evaluated for 5 h, and 2 h of pre-exposure just before the full-scale evaluation was required to stabilize the initial bound. The concentration of NO gas at the beginning of the test was set to 1 ppmv, based on which the reduction performance was evaluated. During the test, the temperature inside the equipment was maintained at 20 °C, and the relative humidity was 50%. The $NO_x$ removal test setup is shown in detail in Fig. 4.

### 2.2.5. *Mechanical tests*

A compressive strength test was conducted in accordance with ASTM C 109 [35], whereas a direct tensile test was performed according to the JSCE recommendation [36]. To evaluate the compressive strength, three 50 × 50 × 50 $mm^3$ specimens were fabricated for each variable. In contrast, to investigate the tensile behavior, a dog-bone-shaped test specimen with a central cross-section measuring 30 × 13 $mm^2$ was fabricated. Five specimens were produced for each variable, whose specific shapes are presented in Fig. 5a.

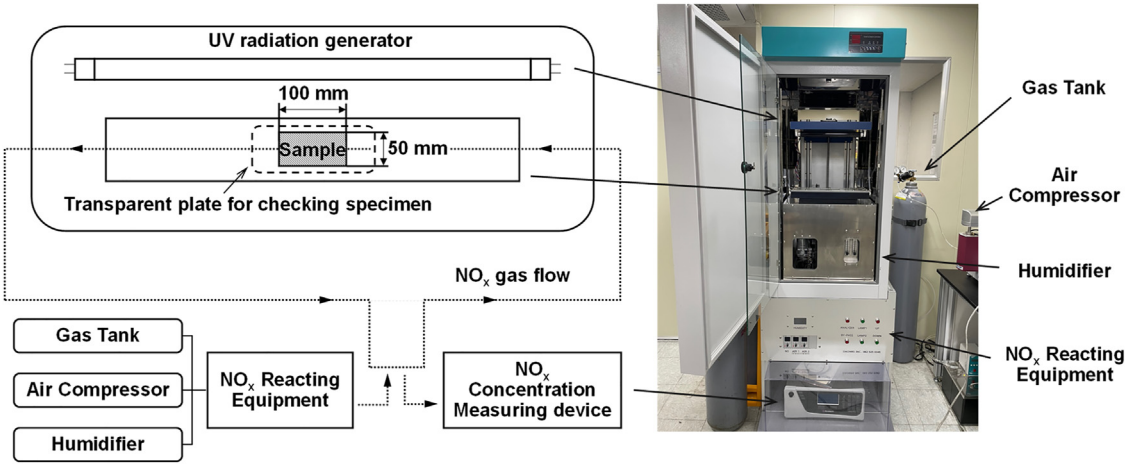


**Fig. 4 – Test Setup of $NO_x$ removal.**

Immediately after the installation of the fresh mixture, the exposed surfaces of all the types of test specimens were covered with polyester film to prevent evaporation of the internal moisture, thereby ensuring a sufficient hydration reaction. As mentioned above, the deforming process was performed after 48 h of dry curing, followed by 7 days of moisture curing in a water tank at 40 °C.

Two types of universal testing machines (UTMs) with different capacities were used for the compressive and tensile tests. The maximum load capacity of the UTM used in the compressive strength test was 3,000 kN, whereas that of the UTM used in the tensile performance test was 250 kN. Loading rates of 0.1 and 0.4 mm/min were adopted for the compressive and tensile tests, respectively. Unlike in the compressive test, where only strength was measured by dividing the maximum applied load by the cross-sectional area of the cube, additional test equipment was required in the tensile test for the tensile strain measurement. The elongation of each specimen was measured using linear variable displacement transformers (LVDTs) fixed to the aluminum frame, and the maximum measurable value of an LVDT was 10 mm, as shown in Fig. 5b. After completion of the tensile test, cracks formed on the

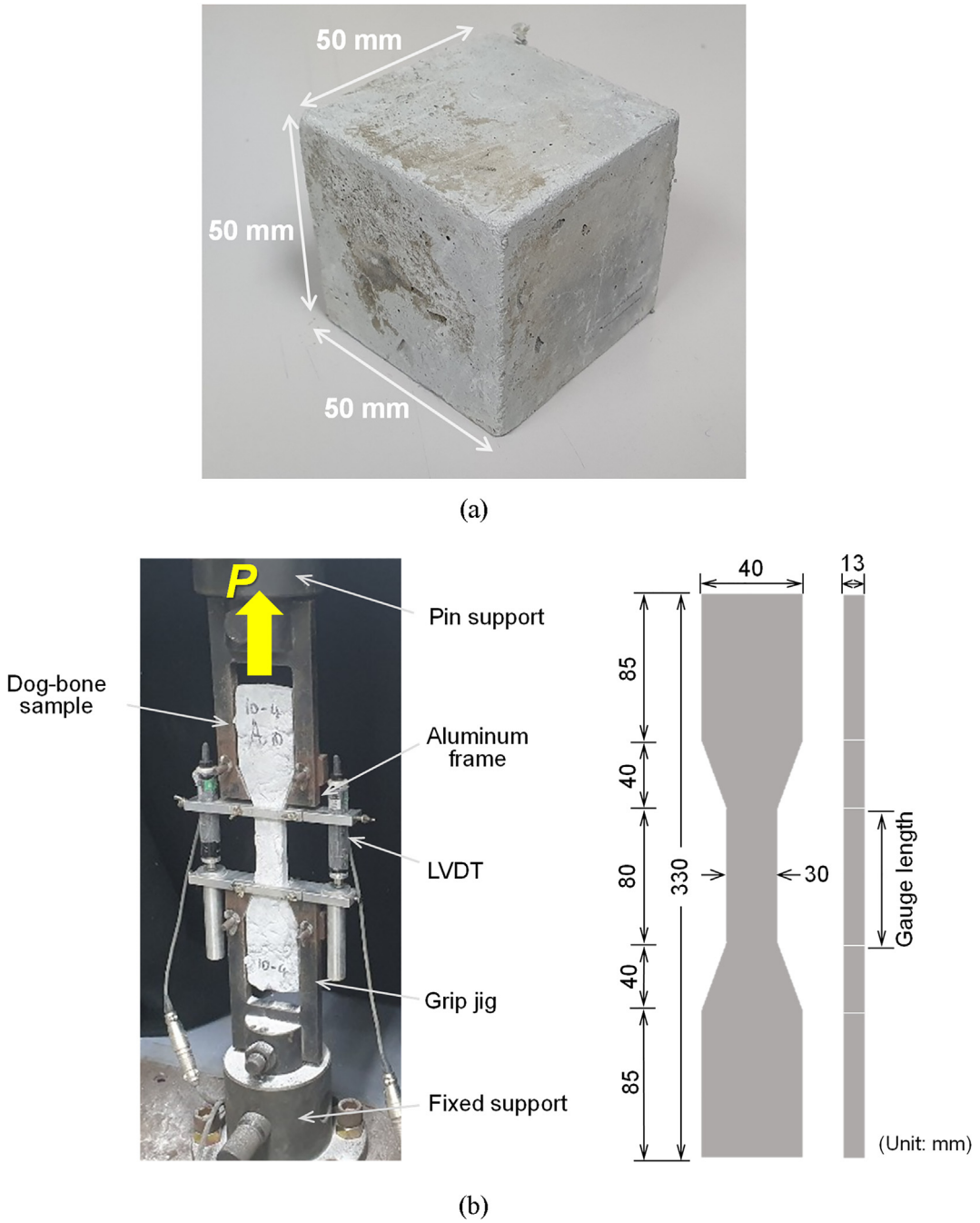


**Fig. 5 – Test setup of (a) compressive strength and (b) tensile behavior.**

specimens were examined; the number of cracks and the distance between the two ends of each crack were measured. From these values, the average length between the cracks was calculated to determine the tendency of each variable to crack, as follows:

$$\text{Average crack spacing (mm)} = D_e/C_{avg}, \quad (1)$$

where $D_e$ indicates the distance between the two ends of the cracks, and $C_{avg}$ indicates the average number of cracks. In addition, microphotographs of the fibers were captured to examine their failure models.

## 3. Determination of optimal amount of VMA

### 3.1. *Effect of VMA on plastic viscosity of white cement mortar*

Rheological properties of specimens are presented in Fig. 6. The plastic viscosity of both U and A specimens tended to increase with the addition of VMA, which is consistent with the findings of Leemann and Winnefeld [37]. The U-1.00% specimen exhibited the highest viscosity, whereas the U-p specimen exhibited the lowest viscosity, which tended to increase with the amount of VMA added. The highest value of 9.91 Pa·s recorded for the U-1.00% specimen was 17% higher than the value of 8.47 Pa·s recorded for the U-p specimen. The second highest plastic viscosity of 9.89 Pa·s was recorded for the U-0.5% specimen, which was slightly lower (by <1%) than the highest value. Compared to that for the U cement type, the increase rate of plastic viscosity obtained via VMA addition was minor for the A cement type. The highest viscosity (9.52 Pa·s) was recorded for the A-0.75% specimen, whereas the A-0.25% specimen achieved the lowest value of 8.39 Pa·s. The second highest value of 9.13 Pa·s was obtained at a VMA content of 0.5%. Thus, it can be concluded that the addition of VMA increases the viscosity of the fresh mixture of cement mortar and is more effective for the U cement type.

### 3.2. *$NO_x$ removal capacity*

Fig. 7 shows the NO gas concentration and time relations of the A and U cement-based samples with the addition of

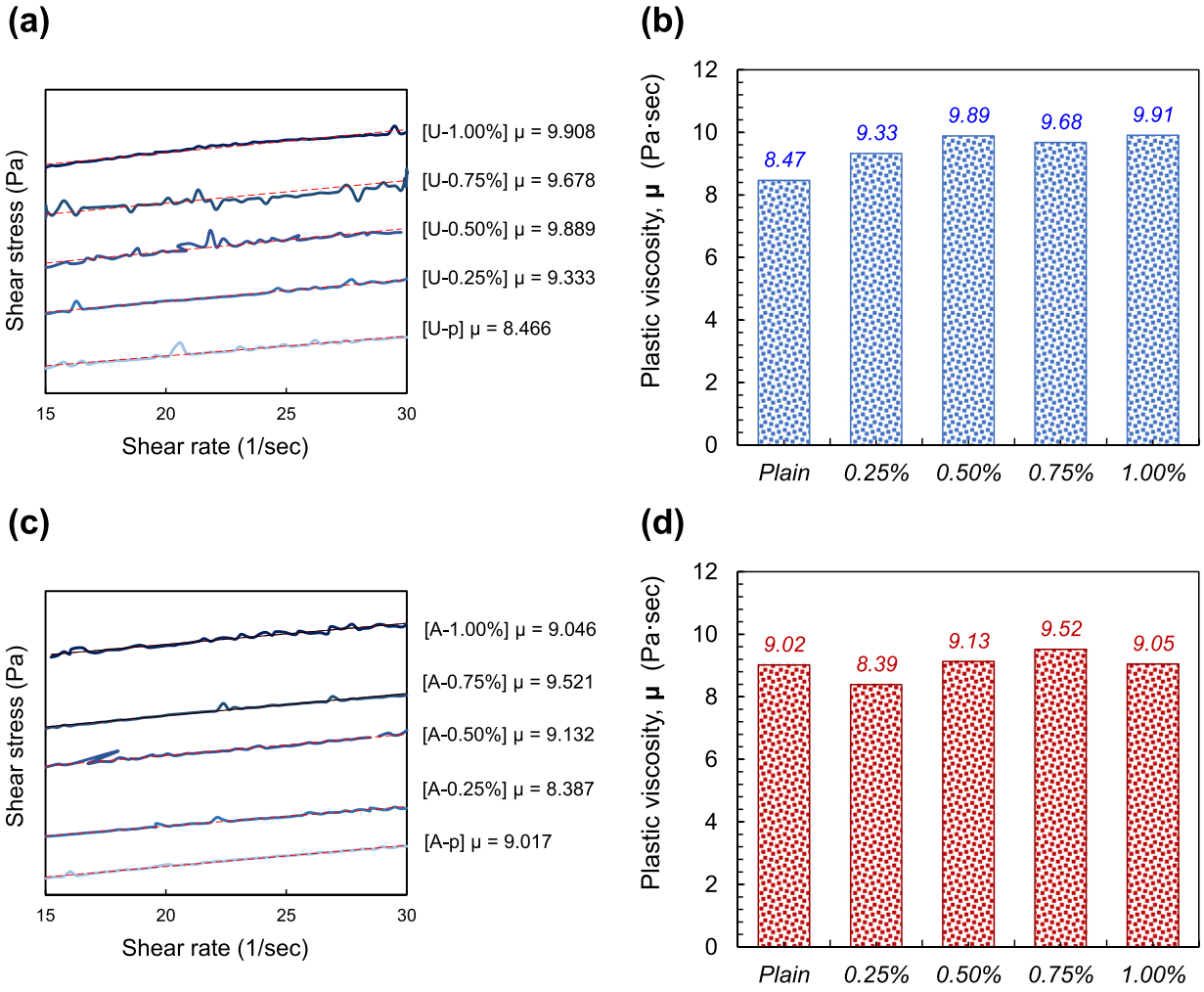


**Fig. 6 – Rheological properties of HPFRCC paste incorporating viscosity agent for various weight content: (a) shear stress–rate curves and (b) plastic viscosity of Union specimens, (c) shear stress–rate curves and (d) plastic viscosity of Aalborg specimens.**

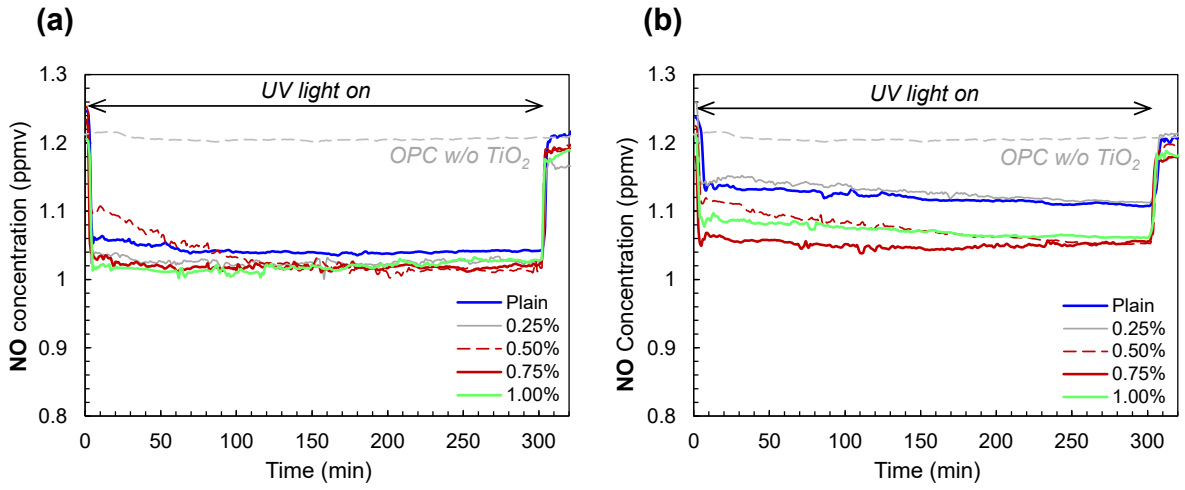


**Fig. 7 – Comparative NO concentration and time behaviors: (a) Union specimens (b) Aalborg specimens.**

various amounts of VMA. The NO gas removal capacities are summarized in Fig. 8. Compared to that of the ordinary Portland cement (OPC) sample without $TiO_2$, the NO gas concentration of $TiO_2$-containing mortar panels evidently decreased under UV irradiation, owing to the photocatalytic action. The NO concentration sharply decreased immediately after the UV light was turned on and then remained constant till the light was turned off. Once the light was turned off, the NO concentration increased owing to the continuous flow of NO gas, which is consistent with previous observations [34,38] and indicates the active photocatalytic reaction of the incorporated $TiO_2$ particles. Park et al. [34] noted that $TiO_2$ first absorbs a photon from the light and generates an EHP. This photon is then converted to a nitrate ion from the water and $O_2$ present in the air, which decreases the NO concentration. For both A and U cement types, when 0.5% of VMA was added, the highest amount of NO was removed (i.e., 5.72 and 8.10 μmol, respectively). The NO removal rates, calculated via dividing the removed NO gas by the input NO gas, were 12.4% and 17.3%, respectively, in the cases of A- and U-0.5%. In the case of A cement, a higher NO removal capacity was achieved by adding VMA, whereas 0.5% and 0.75% VMA contents were only effective in improving the NO removal capacity of U-based mortar.

Fig. 9 shows the relation between the NO removal capacity and plastic viscosity. There is a minor correlation between the plastic viscosity of the cement mortar and its NO removal capacity, which is attributable to the sufficient viscosity of the mortar mixture used in this study. This is supported by the results obtained by Li and Li [24], who reported that the fiber dispersion coefficient in engineered cementitious composites (ECCs) increases with the plastic viscosity but shows a plateau-like trend after the Marsh cone flow time reaches 24 s. They [24] suggested a simple equation for the relation between the plastic viscosity ($x$) and Marsh cone flow time ($y$): $y = 2.3737x + 5.9715$. The minimum and maximum plastic viscosities obtained were 8.39 and 9.91 Pa·s, respectively, corresponding to the Marsh cone flow time periods of

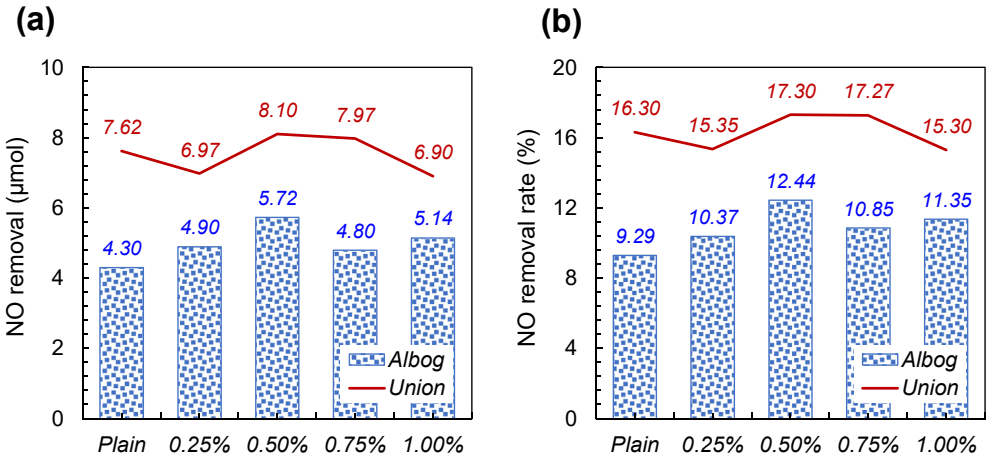


**Fig. 8 – NO removal comparisons.**

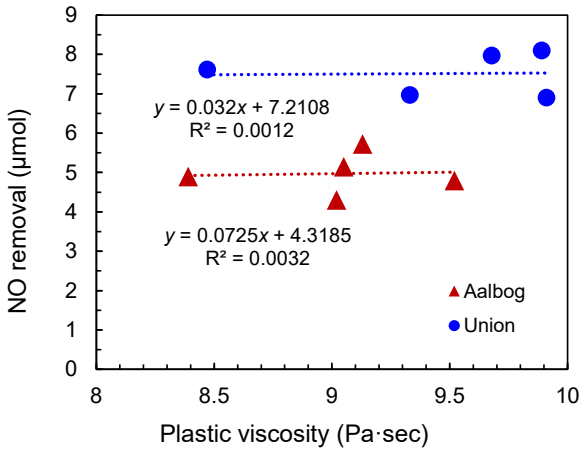


**Fig. 9 – Relation between NO removal and plastic viscosity.**

25.9 and 29.5 s, according to the suggested equation. This means that the viscosity of the cement mortar considered for producing HPFRCCs was sufficiently high owing to its low W/B value and high amount of fineness ingredients. The increased plastic viscosity is generally effective in improving the dispersibility of fibers; however, it also leads to larger sizes and amounts of entrapped air pores, which result in lower net cross-sectional areas and amounts of fibers in the weakest zone [24]. For these reasons, the dispersibility of $TiO_2$ particles did not linearly increase with plastic viscosity, and there was a minor correlation between the NO removal capacity and plastic viscosity.

Compared to A cement, U cement showed better NO removal through the photocatalytic action of $TiO_2$ particles at all ranges of VMA contents. For example, the NO removal of U white cement-based mortar was approximately 51% higher than that of A white cement-based mortar on average. Guo and Poon [7] noted that a higher light absorption of OPC results in fewer EHPs, which mitigates the NO removal capacity of $TiO_2$ particles. Among the two types of white cement, the U cement is recommended for use in terms of the NO removal capacity of cement mortar, compared to the A cement. In addition, based on the NO removal test results, the most appropriate amount of VMA for both A and U white cement cases, in terms of both performance and efficiency, was determined to be 0.5%. When the input amount of VMA exceeds 0.5%, the efficiency of NO removal rather decreased because the flowability of composite already significantly reduced due to utilization of $TiO_2$. Thus, it was decided to add an equal amount of VMA to 0.5% of the weight of cement for the tests conducted for evaluating the mechanical performance.

## 4. Determination of appropriate fiber treatment method through mechanical properties

### 4.1. *Compressive strength*

The compressive strengths of the two cement specimens are presented in Fig. 10. The difference between the highest compressive strength (91.8 MPa) and lowest strength (85.6 MPa) was only approximately 6.2 MPa for the U cement type (Fig. 10a). This means that the surface treatment method of the PE fiber insignificantly influences the compressive strength of HPFRCCs. Although the lowest value was achieved for the U-M specimen, the plasma coating specimens with a single gas type showed a higher compressive strength than that of the others: only U–Ar and U–O specimens showed a compressive strength above 90 MPa. Compared to those for the U cement type, slightly lower compressive strengths were obtained for the A cement samples. One potential reason for this is the lower viscosity of the A cement samples (Fig. 6), which limits the uniform dispersion of the PE fibers in the matrix. The HPFRCC samples having undergone plasma treatment and chromic acid treatments for 5 min exhibited similar compressive strengths, while those subjected to 10-min chromic acid treatment exhibited the highest compressive strength of 91.5 MPa. Owing to the worse fiber dispersibility, larger data deviations were found in the A cement samples.

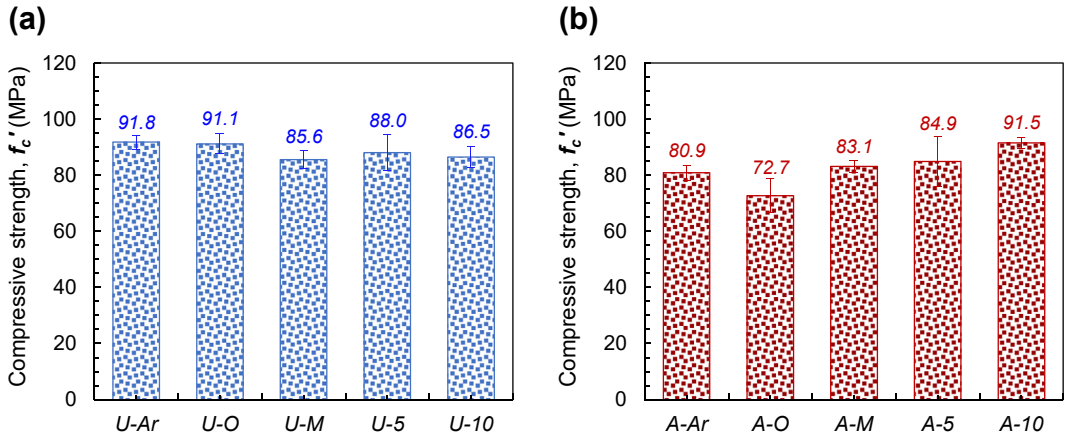


**Fig. 10 – Compressive strength of HPFRCC using surface-treated PE fiber of (a) Union specimens and (b) Aalborg specimens.**

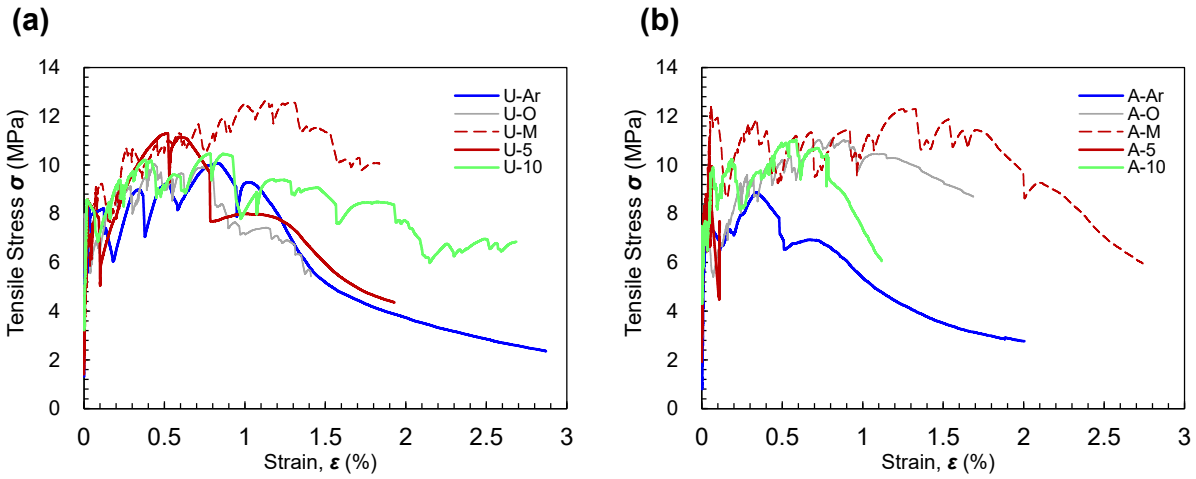


**Fig. 11 – Comparative tensile stress versus strain curves of HPFRCC using surface-treated PE fiber of (a) Union specimens and (b) Aalborg specimens.**

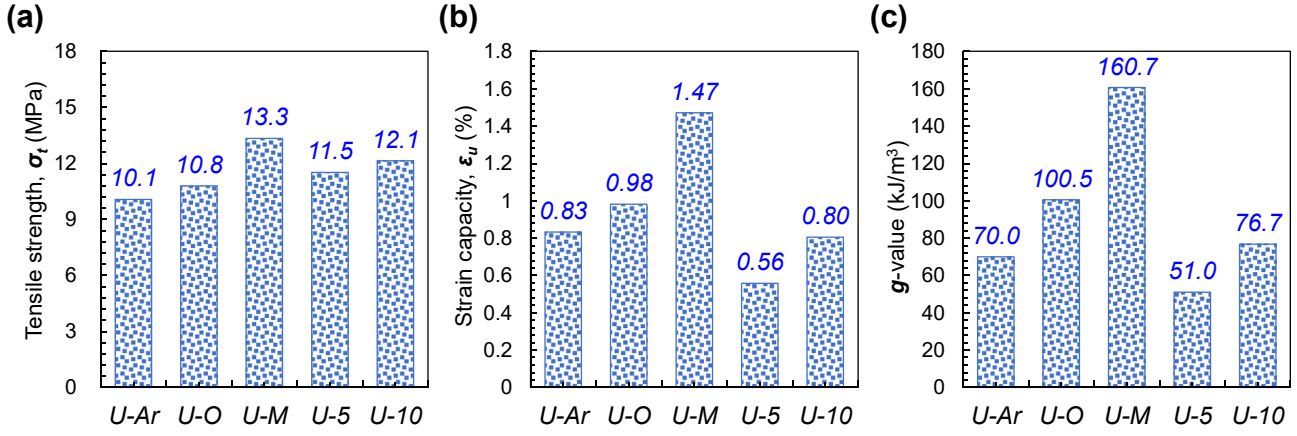


**Fig. 12 – Summary of tensile parameters for Union specimens: (a) tensile strength, (b) strain capacity, (c) g-value.**

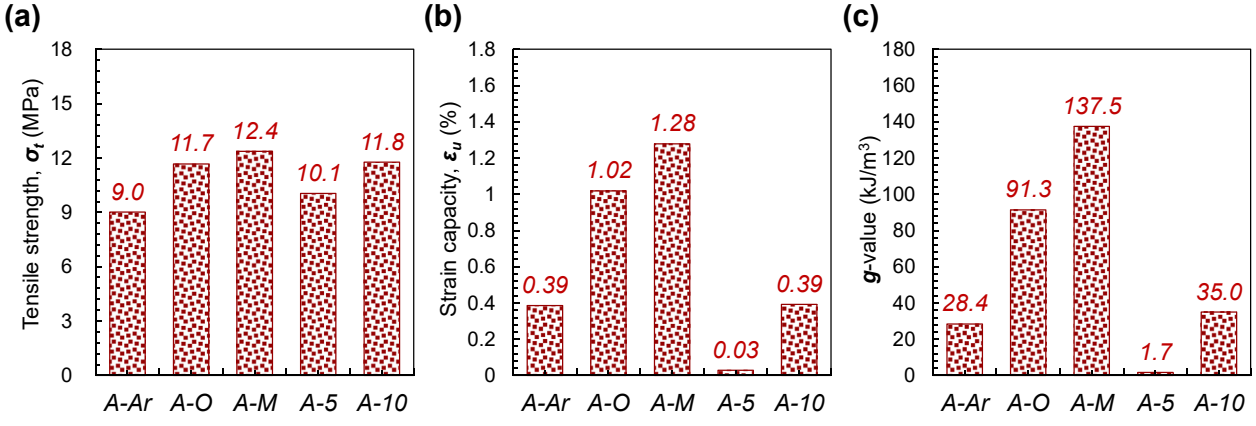


**Fig. 13 – Summary of tensile parameters for Aalborg specimens: (a) tensile strength, (b) strain capacity, (c) g-value.**

Felekoglu et al. [32] reported that cementitious composites containing plasma-treated polypropylene fibers on the surface exhibited higher flexural strength than that in plain specimens. In particular, the flexural strength was the highest in the specimen that used Ar during plasma treatment. Payrow et al. [39] noted that the effect of chromic acid treatment for polymer fibers on the compressive strength of concrete incorporating fibers was negligible. Yoo et al. [40] reported a significant increase in the compressive strength of a rapidly hardening mortar when using surface-treated PE fibers. The compressive strength evaluation presented in this study does not indicate a dramatic difference from the previous studies [32,39,40]. These results are attributed to the dense matrix of an HPFRCC. Based on this consideration, the compressive strength of an HPFRCC is considered to be affected more by the specific properties of the matrix (such as the viscosity of the composite) than the surface condition of the incorporated fiber.

### 4.2. *Tensile behaviors*

Fig. 11 shows the tensile stress–strain curves of specimens separated according to the cement type, and Figs. 12 and 13 show several parameters related to their tensile performance. Unlike the compressive strength measurements, the tensile test measurements showed a distinct tendency regardless of the cement type. Among the U cement variables, the U-M specimen exhibited outstanding performance for all parameters. The U-M specimen had the highest tensile strength (13.3 MPa), which was approximately 10% higher than the second highest value (12.1 MPa) recorded for the U-10 specimen and approximately 33% higher than the lowest value (10.1 MPa) recorded for the U–Ar specimen. In case of the strain capacity, the U-M specimen exhibited the highest value of 1.47%, which was 50% higher than the second highest value of 0.98% recorded for the U–O specimen and 164% higher than the lowest value of 0.56% recorded for the U-5 specimen. The highest tensile strength (12.4 MPa) was achieved by the A-M specimen, which was 5% higher than the second highest value of 11.8 MPa recorded for the A-10 specimen and 23% higher than the lowest value of 10.1 MPa recorded for the A-Ar specimen. In addition, among the A cement specimens, the A-M specimen exhibited the highest strain capacity of 1.28%, which was approximately 25% higher than the second highest value of 1.02% recorded for the A-O specimen.

As a result, the U- and A-M specimens achieved the highest energy absorption capacity up to the peak (called $g$-value). For instance, the recorded $g$-values were 160.7 and 137.5 kJ/m$^3$, respectively, for the U-M and A-M specimens. The highest performance level of fiber-reinforced concrete is known to have a $g$-value exceeding 50 kJ/m$^3$ [41]. In addition, ECC, which is one of the best strain-hardening cement composites, exhibits a $g$-value of 148 kJ/m$^3$ [42]. Thus, the photocatalytic HPFRCC containing the plasma-treated PE fibers could absorb energy, similar to the case of ECC. Regardless of the white cement type, the $O_2$-gas plasma-treated fiber samples yielded the second-best energy absorption capacity, followed by the Ar–gas plasma-treated fiber samples. This is attributable to the higher surface oxidation. Tosun et al. [43] reported that $O_2$-gas and Ar–gas increase the bond between cement matrix and fiber through different mechanisms. Plasma treatment cleaves the C–C/C–H bonds and creates oxygen-containing functional groups in the molecular chain of the surface of PE fibers. Thus, the $O_2$-gas plasma treatment was more effective in incorporating the oxygen-containing functional groups, which helped to disperse the PE fibers in the mixture and increase their chemical bond to the cement matrix. On the other hand, Ar–gas plasma treatment was more effective in improving nano-roughness of the fiber surface, which led to improve physical bond [43]. Comparing the two cases, it was the formation of oxygen-containing functional groups rather than the improvement in nano-roughness that had a greater impact on tensile performance of HPFRCCs. Consequently, a remarkable point of this study is that using the mixed gas simultaneously increases physical and chemical bond between cement matrix and fiber, which brought about positive synergies to achieve better tensile performance than the case of using single gas. Worse tensile properties were obtained for the chromic-acid-treated PE fiber samples. In particular, the 5-min chromic acid-treated fiber samples yielded the lowest $g$-values, which increased with the treatment time increased to 10 min. Such an improved energy absorption capacity of HPFRCCs obtained by increasing the time of chromic acid treatment was potentially caused by the highly oxidized PE fiber surface. Yoo et al. [44] reported that the O/C atomic ratio increased from 10.8% to 17.4% with an increase in the chromic acid treatment time from 5 to 10 min; they also reported the enhanced tensile properties of strain-hardening cementitious composites owing to the increased treatment time of chromic acid. The insufficient surface oxidation but highly roughened surface and fibrillation of the U- and A-5 specimens can limit further increases in the tensile stress and deformability, resulting in the worst energy absorbing capacity.

To validate the achieved tensile performance, the fiber states located at the localized crack plane were analyzed through SEM images. Fig. 14 presents the surface states of the pulled-out PE fibers from the cement matrix. More severe scratches were observed on the surface of the fiber acquired from the specimen, which yielded a higher tensile performance. In particular, fibers extracted from U- and A-M specimens exhibited a certain level of deformation because of the intense scratches produced by the adherent fine matrix particles at the interfacial zone. However, the fibers obtained from the U- and A-5 specimens, which exhibited extremely low tensile performance, had smooth surfaces without noticeable surface abrasion, indicating the presence of insufficient interfacial shear resistance required to suppress the fiber pull-out.

### 4.3. *Crack patterns*

Figs. 15 and 16 illustrate the multi-cracked samples obtained after the completion of the tensile test, and Fig. 17 presents the crack parameters. The trend of the number of cracks was quite similar to that of the $g$-value acquired from the tensile test. The average number of cracks on the specimens

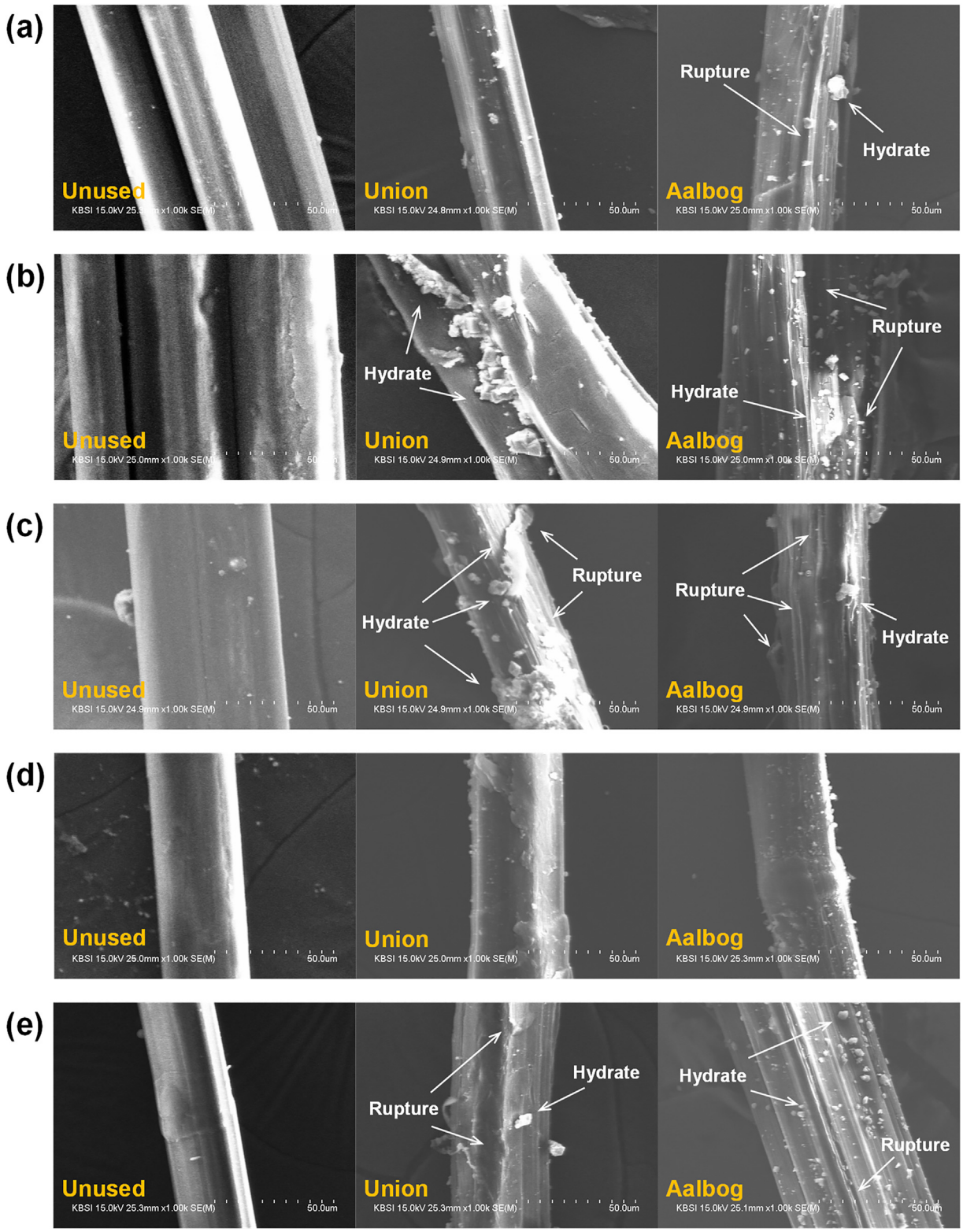


**Fig. 14 – SEM images of pulled out PE fibers: (a) Argon plasma treated, (b) Oxygen plasma treated, (c) Mixed gas plasma treated, (d) Chromic acid 5 min. treated, (e) Chromic acid 10 min. treated.**

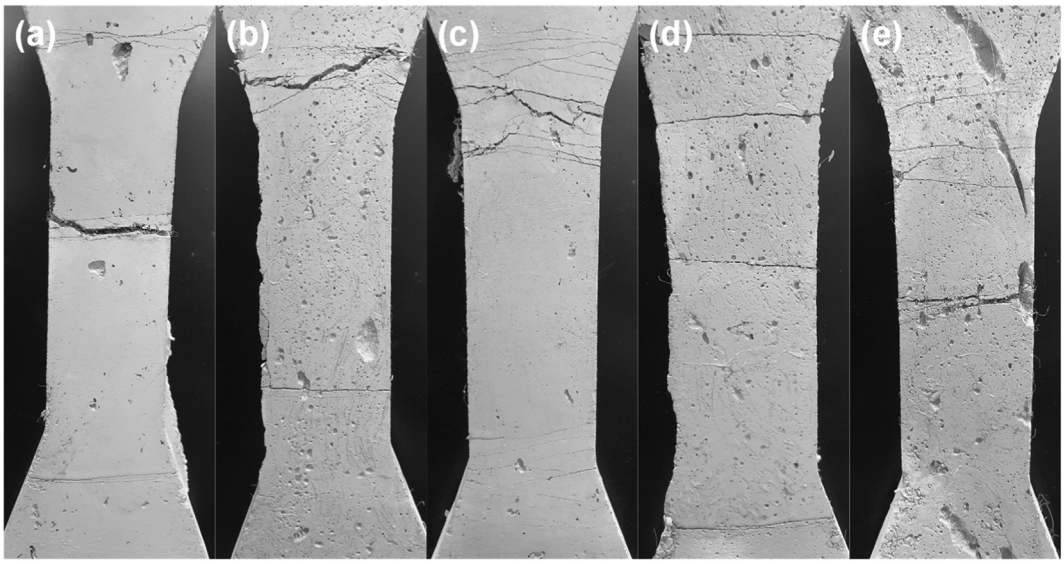


**Fig. 15 – Crack patterns for Union specimens: (a) U–Ar, (b) U–O, (c) U-M, (d) U-5, and (e) U-10.**

containing PE fibers treated by mixed-gas plasma yielded the highest value. The U-M sample produced 15.2 cracks on average, whereas the A-M sample produced 13.6 cracks. This multiple cracking behavior verified the strain-hardening behavior under tension. Additional cracks in the matrix can be formed when the tensile stress transferred through the fiber–matrix interfacial bond exceeds its tensile strength. Thus, multiple crack formation indicates excellent fiber bridging strength, allowing the transfer of higher tensile stresses to the surrounding matrix. Among the U cement specimens, the least average cracks (3.2) were observed for U-5. In contrast, the A-Ar and A-5 samples possessed equal numbers of least average cracks (2.8) for the A cement samples. The number of cracks was inversely proportional to the average crack spacing. The lowest average crack spacing (7.9 mm) was observed for the U-M specimen, the minimum among the U cement cases, which confirmed that the cracks occurred most closely in this specimen. The lowest average crack spacing was reported for the A-5 specimen among the A cement variables, which is attributable to the fact that the cracks were concentrated in a certain part because of early failure. The corresponding fiber fracture pattern is shown in Fig. 18. Excluding the exception corresponding to the A-5 specimen, the average distance between the cracks in the A-M specimen was the narrowest (8.8 mm) in the A cement case. The most probable reason for the crack concentration identified in several specimens was poor fiber dispersion. $TiO_2$ reduced the flowability of specimens, which led to deterioration of fiber dispersibility. To improve the fiber dispersion capacity, further research needs to be conducted.

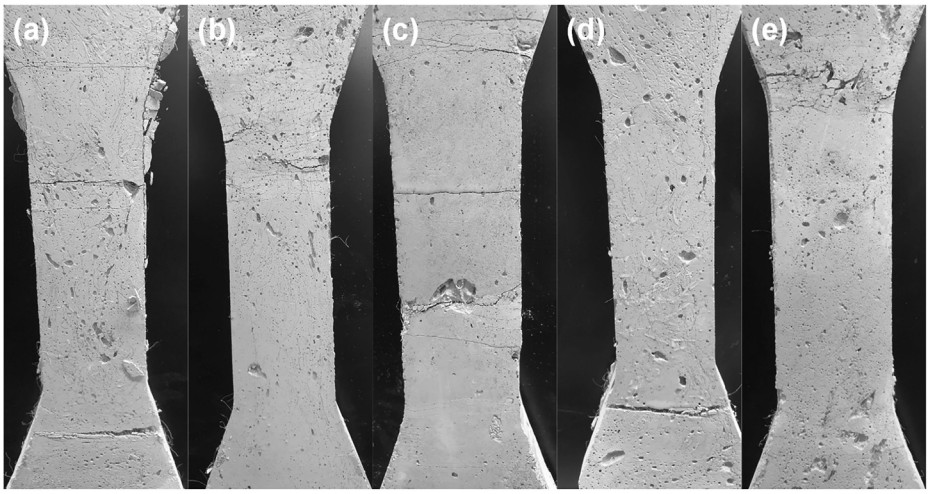


**Fig. 16 – Crack patterns for Aalborg specimens: (a) A-Ar, (b) A-O, (c) A-M, (d) A-5, and (e) A-10.**

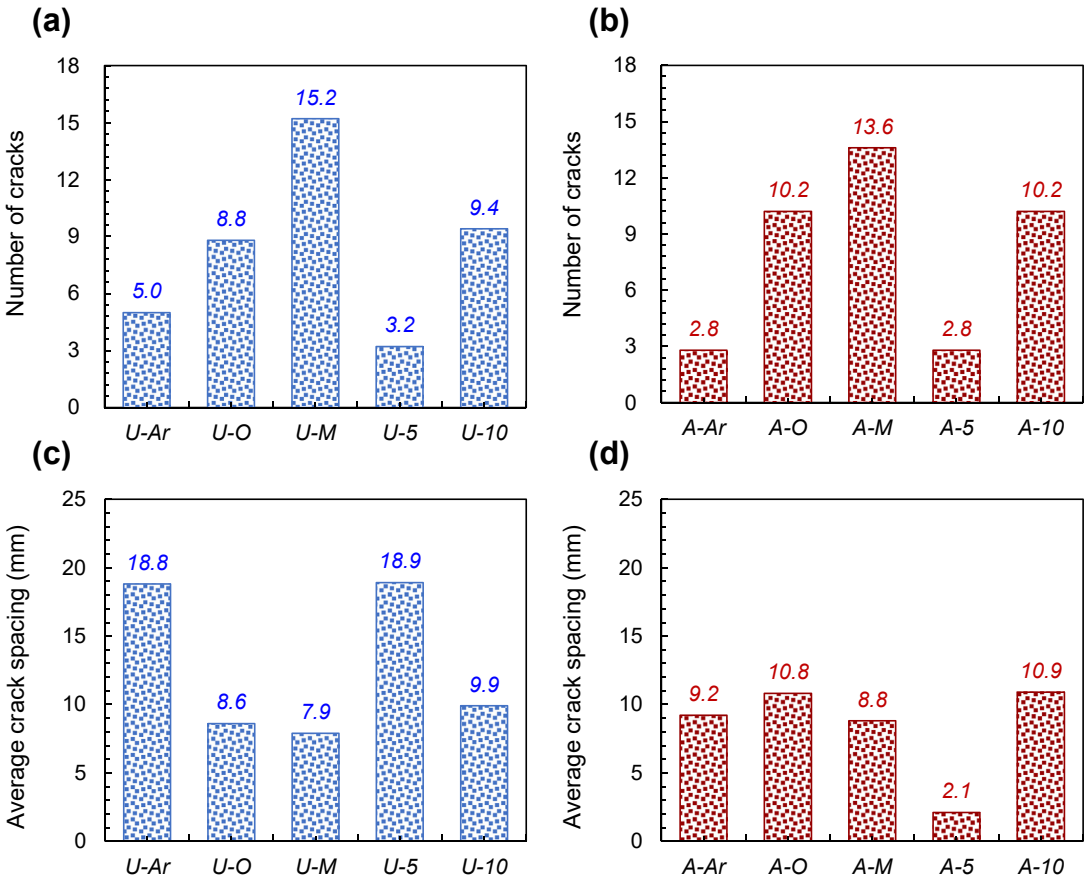


**Fig. 17 – Summary of crack patterns.**

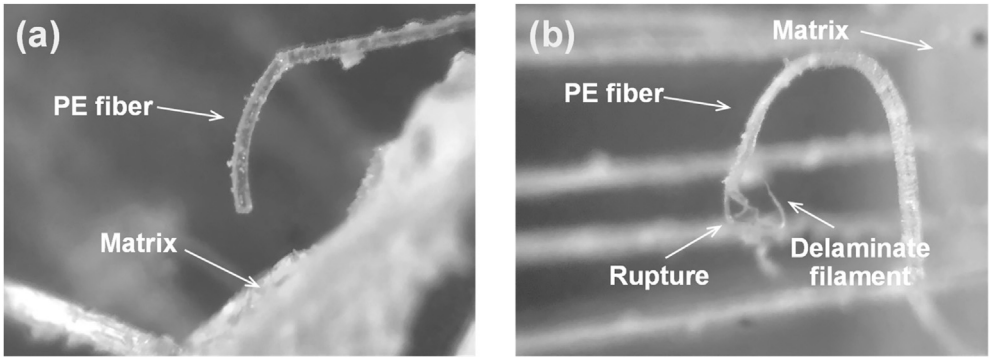


**Fig. 18 – Examples of fiber fracture pattern: (a) completely pulled out fiber from A-M specimen, (b) failed fiber from A-5 specimen.**

## 5. Conclusions

This study determined the optimal amount of VMA and an appropriate fiber treatment method required to increase the $NO_x$ removal capacity and mechanical properties of HPFRCCs containing white Portland cement and $TiO_2$ powder. Based on the test results and the above discussion, the following conclusions can be drawn.

1) The plastic viscosity of the cement mortar tended to increase with VMA addition. Owing to the sufficient viscosity of the plain mortar, no correlation between the NO removal efficiency and plastic viscosity existed according to the amount of VMA.
2) The $TiO_2$-containing mortar showed an evident decrease in NO gas concentrations up to 17.3%. As 0.5% VMA was added, the highest amounts of NO gas could be removed

for both Aalborg and Union cement types (i.e., 5.72 and 8.10 μmol, respectively).

3) Union cement was more effective in removing NO gas through the photocatalytic action of $TiO_2$ particles than the Aalborg cement under all ranges of VMA content. It also achieved a higher compressive strength than that of its counterpart.
4) The compressive strength of HPFRCCs was influenced by the surface treatment method of the PE fiber; however, the difference was insignificant. The compressive strength of the tested photocatalytic HPFRCCs was determined as 72.7–91.8 MPa.
5) In contrast to the compressive tests, the tensile tests showed a significant difference in the performance parameters between each variable depending on the treatment method used. For both cement types, the plasma treatment of the hybrid Ar–gas and $O_2$-gas (i.e., the U-M and A-M specimens) yielded the optimal tensile performance, whereas the specimens subjected to chromic acid treatment exhibited worse tensile performance. The Ar- and $O_2$-gas-based plasma treatments exhibited intermediate performance.
6) The number of cracks tended to show similar trends with the *g*-value, meaning that the hybrid Ar- and $O_2$-gas-based plasma treatment produced the maximum microcracks, owing to its excellent fiber bridging capacity.

## Declaration of Competing Interest

There is no conflict of interest.

## Acknowledgements

This work was supported by the Construction Technology Research Project (21SCIP–B149189-04) funded by the Ministry of Land, Infrastructure and Transport.

## Appendix A

The average values and standard deviation of mechanical properties (compressive strength, tensile strength, strain capacity, and g-value) are summarized in Table A1.

## REFERENCES

[1] Sugrañez R, Álvarez JI, Cruz-Yusta M, Mármol I, Morales J, Vila J, et al. Enhanced photocatalytic degradation of $NO_x$ gases by regulating the microstructure of mortar cement modified with titanium dioxide. Build Environ 2013;69:55–63.
[2] Yang L, Hakki A, Wang F, Macphee DE. Photocatalyst efficiencies in concrete technology: the effect of photocatalyst placement. Appl Catal B Environ 2018;222:200–8.
[3] Jalal M, Fathi M, Farzad M. Effects of fly ash and $TiO_2$ nanoparticles on rheological, mechanical, microstructural and thermal properties of high strength self compacting concrete. Mech Mater 2013;61:11–27.
[4] Zhang R, Cheng X, Hou P, Ye Z. Influences of nano-$TiO_2$ on the properties of cement-based materials: hydration and drying shrinkage. Constr Build Mater 2015;81:35–41.
[5] Jimenez-Relinque E, Rodriguez-Garcia JR, Castillo A, Castellote M. Characteristics and efficiency of photocatalytic cementitious materials: type of binder, roughness and microstructure. Cem Concr Res 2015;71:124–31.
[6] Rhee I, Lee J-S, Kim J, Kim J-H. Nitrogen oxides mitigation efficiency of cementitious materials incorporated with $TiO_2$. Materials (Basel) 2018;11:877.
[7] Guo M-Z, Poon CS. Superior photocatalytic $NO_x$ removal of cementitious materials prepared with white cement over ordinary Portland cement and the underlying mechanisms. Cem Concr Compos 2018;90:42–9.
[8] Reda M, Shrive N, Gillott J. Microstructural investigation of innovative UHPC. Cem Concr Res 1999;29:323–9.
[9] Wille K, Naaman AE. Pullout behavior of high-strength steel fibers embedded in ultra-high-performance concrete. ACI Mater J 2012;109:479–88.
[10] Yoo D-Y, Yoon Y-S. A review on structural behavior, design, and application of ultra-high-performance fiber-reinforced concrete. Int J Concr Struct Mater 2016;10:125–42.
[11] Kang S-T, Lee Y, Park Y-D, Kim J-K. Tensile fracture properties of an ultra high performance fiber reinforced concrete (UHPFRC) with steel fiber. Compos Struct 2010;92:61–71.
[12] Fu X, Chung DDL. Bond strength and contact electrical resistivity between cement and stainless steel fiber: their correlation and dependence on fiber surface treatment and curing age. ACI Mater J 1997;94:203–8.
[13] Wu H-C, Li VC. Fiber/cement interface tailoring with plasma treatment. Cem Concr Compos 1999;21:205–12.
[14] Pi Z, Xiao H, Du J, Liu M, Li H. Interfacial microstructure and bond strength of nano-$SiO_2$-coated steel fibers in cement matrix. Cem Concr Compos 2019;103:1–10.

**Table A1 – Summary of mechanical test results of HPFRCCs.**

| Specimen | Compressive strength $f_c'$ [MPa] | Tensile strength $f_t$ [MPa] | Strain capacity $\epsilon_u$ [%] | *g*-value [kJ/m$^3$] |
|---|---|---|---|---|
| U–Ar | **91.8** (7.4) | **10.1** (0.6) | **0.83** (0.00) | **70.0** (3.7) |
| U–O | **91.1** (10.7) | **10.8** (2.2) | **0.98** (0.66) | **100.5** (79.4) |
| U-M | **85.6** (8.7) | **13.3** (0.8) | **1.47** (0.37) | **160.7** (50.5) |
| U-5 | **88.0** (18.5) | **11.5** (0.9) | **0.56** (0.11) | **51.0** (10.6) |
| U-10 | **86.5** (10.6) | **12.1** (1.3) | **0.80** (0.57) | **76.7** (57.0) |
| A-Ar | **80.9** (7.7) | **9.0** (1.6) | **0.39** (0.08) | **28.4** (3.3) |
| A-O | **72.7** (17.5) | **11.7** (1.9) | **1.02** (0.42) | **91.3** (23.9) |
| A-M | **83.1** (5.6) | **12.4** (0.7) | **1.28** (0.08) | **137.5** (12.3) |
| A-5 | **84.9** (20.5) | **10.1** (1.7) | **0.03** (0.02) | **1.7** (1.1) |
| A-10 | **91.5** (5.9) | **11.8** (0.6) | **0.39** (0.30) | **35.0** (26.8) |

*Bold = average value and parentheses () = standard deviation.

[15] Yoo D-Y, Shin W, Chun B. Corrosion effect on tensile behavior of ultra-high-performance concrete reinforced with straight steel fibers. Cem Concr Compos 2020;109:103566.
[16] Yoo D-Y, Jang YS, Chun B, Kim S. Chelate effect on fiber surface morphology and its benefits on pullout and tensile behaviors of ultra-high-performance concrete. Cem Concr Compos 2021;115:103864.
[17] Yoo D-Y, Kim M-J. High energy absorbent ultra-high-performance concrete with hybrid steel and polyethylene fibers. Constr Build Mater 2019;209:354–63.
[18] Feldman D, Denes F, Zeng Z, Denes AR, Banu D. Polypropylene fiber–matrix bonds in cementitious composites. J Adhes Sci Technol 2000;14:1705–21.
[19] Wei Q. Surface characterization of plasma-treated polypropylene fibers. Mater Char 2004;52:231–5.
[20] Yang E-H, Li VC. Strain-hardening fiber cement optimization and component tailoring by means of a micromechanical model. Constr Build Mater 2010;24:130–9.
[21] Mercado-Cabrera A, Jaramillo-Sierra B, López-Callejas R, Valencia-Alvarado R, de la Piedad-Beneitez A, Peña-Eguiluz R, et al. Surface modification of polypropylene fiber for hydrophilicity enhancement aided by DBD plasma. Prog Org Coating 2013;76:1858–62.
[22] Kang S-T, Kim J-K. The relation between fiber orientation and tensile behavior in an ultra high performance fiber reinforced cementitious composites (UHPFRCC). Cem Concr Res 2011;41:1001–14.
[23] Yoo D-Y, Lee J-H, Yoon Y-S. Effect of fiber content on mechanical and fracture properties of ultra high performance fiber reinforced cementitious composites. Compos Struct 2013;106:742–53.
[24] Li M, Li VC. Rheology, fiber dispersion, and robust properties of engineered cementitious composites. Mater Struct 2013;46:405–20.
[25] Lucas SS, Ferreira VM, de Aguiar JLB. Incorporation of titanium dioxide nanoparticles in mortars — influence of microstructure in the hardened state properties and photocatalytic activity. Cem Concr Res 2013;43:112–20.
[26] Yang L, Wang F, Shu C, Liu P, Zhang W, Hu S. $TiO_2$/porous cementitious composites: influences of porosities and $TiO_2$ loading levels on photocatalytic degradation of gaseous benzene. Constr Build Mater 2017;150:774–80.
[27] Choi H-J, Oh T, Yoo D-Y. Enhancing fiber–matrix interfacial bond in ultra-high-performance concrete containing titanium dioxide. Mater Lett 2020;280:128547.
[28] Lachemi M, Hossain KM, Lambros V, Nkinamubanzi P-C, Bouzoubaâ N. Performance of new viscosity modifying admixtures in enhancing the rheological properties of cement paste. Cem Concr Res 2004;34:185–93.
[29] Meng W, Khayat KH. Improving flexural performance of ultra-high-performance concrete by rheology control of suspending mortar. Compos B Eng 2017;117:26–34.
[30] Devaux E, Cazé C. Composites of UHMW polyethylene fibres in a LD polyethylene matrix. I. Processing conditions. Compos Sci Technol 1999;59:459–66.
[31] Kanda T, Li VC. Interface property and apparent strength of high-strength hydrophilic fiber in cement matrix. J Mater Civ Eng 1998;10:5–13.
[32] Felekoglu B, Tosun K, Baradan B. A comparative study on the flexural performance of plasma treated polypropylene fiber reinforced cementitious composites. J Mater Process Technol 2009;209:5133–44.
[33] ISO-22197. Fine ceramics (advanced ceramics, advanced technical ceramics) - test method for air-purification performance of semiconducting photocatalytic materials. 2016.
[34] Park J-J, Kim S, Shin W, Choi H-J, Park G-J, Yoo D-Y. High-performance photocatalytic cementitious materials containing synthetic fibers and shrinkage-reducing admixture. Materials (Basel) 2020;13:1828.
[35] ASTM C109/C109M-16a, Standard test method for compressive strength of hydraulic cement mortars (Using 2-in . or [50-mm] cube specimens). 2016.
[36] JSCE. Recommendations for design and construction of high performance fiber reinforced cement composites with multiple fine cracks (HPFRCC). 2008.
[37] Leemann A, Winnefeld F. The effect of viscosity modifying agents on mortar and concrete. Cem Concr Compos 2007;29:341–9.
[38] Seo D, Yun TS. $NO_x$ removal rate of photocatalytic cementitious materials with $TiO_2$ in wet condition. Build Environ 2017;112:233–40.
[39] Payrow P, Nokken MR, Banu D, Feldman D. Effect of surface treatment on the post-peak residual strength and toughness of polypropylene/polyethylene-blended fiber-reinforced concrete. J Compos Mater 2011;45:2047–54.
[40] Yoo D-Y, Oh T, Chun B. Highly ductile ultra-rapid-hardening mortar containing oxidized polyethylene fibers. Constr Build Mater 2021;277:122317.
[41] Wille K, El-Tawil S, Naaman AE. Properties of strain hardening ultra high performance fiber reinforced concrete (UHP-FRC) under direct tensile loading. Cem Concr Compos 2014;48:53–66.
[42] Ranade R, Stults MD, Li VC, Rushing TS, Roth J, Heard WF. Development of high strength high ductility concrete. In: 2nd Int. RILEM Conf. Strain Hardening Cem. Compos.; 2011. p. 1–8.
[43] Tosun K, Felekoğlu B, Baradan B. Multiple cracking response of plasma treated polyethylene fiber reinforced cementitious composites under flexural loading. Cem Concr Compos 2012;34:508–20.
[44] Yoo D-Y, Oh T, Kang M-C, Kim M-J, Choi H-J. Enhanced tensile ductility and sustainability of high-strength strain-hardening cementitious composites using waste cement kiln dust and oxidized polyethylene fibers. Cem Concr Compos 2021;120:104030.